Design and analysis of a thick Miura-ori folded structure with large negative Poisson's ratio

Moradweysi P.[a], Santucci P.M.[b], Carta G.[b,*], Goudarzi T.[a], Aghdam M.M.[a], Baldi A.[b], Brun M.[b]

[a]Department of Mechanical Engineering, Amirkabir University of Technology (Tehran Polytechnic), Hafez Ave, Tehran, 15916-34311, Iran
[b]Department of Mechanical, Chemical and Materials Engineering, University of Cagliari, Piazza d'Armi, Cagliari, 09123, Italy

Abstract

In this paper, effective properties of Miura-ori patterned sheets are studied. The thickness of the facets is allowed to have considerably large values, hence the structural response of the system cannot be determined by considering only the kinematics of the folding. In particular, large negative values of the Poisson's ratio have been observed for particular sets of parameters. Numerical outcomes, for periodic and finite systems, have been validated by an experimental campaign, where several specimens with different geometries and materials have been tested. The elastic fields of the specimens have been measured with the Digital Image Correlation method.

*Corresponding author (e-mail address: giorgio_carta@unica.it)

Keywords: Negative Poisson's ratio, auxetic structure, Miura-ori folded sheet, metamaterial, Digital Image Correlation.

1

1 Introduction

Auxetic media are characterised by a negative value of Poisson's ratio, namely they expand (or contract) laterally when stretched (or compressed) longitudinally. The term *auxetic*, firstly used by Evans in this context, derives from the Greek word "auxetos", which means "that may be increased" [27]. The Poisson's ratio of an isotropic material is in the range $(-1, 0.5)$, while for an anisotropic medium both the lower and upper limits cease to hold [98].

Auxetic materials offer enhanced performance for many engineering applications in comparison with traditional materials. In terms of mechanical properties, auxeticity can be exploited to obtain higher indentation resistance [15, 28], increased fracture toughness [49, 19] and longer fatigue life [30]. Auxetic systems can also be employed to achieve either enhanced energy dissipation [86, 31, 114, 70] or improved acoustic energy harvesting [54, 25]. In addition, auxetic structures can deform into dome shapes when subjected to bending, thus exhibiting synclastic curvature instead of the typical anticlastic curvature of common structures [24, 67].

Due to their increasing potentialities, the use of auxetic media has been proposed in different fields. For instance, medical devices based on auxetic technology, such as dilators to open arteries in case of coronary angioplasty [109, 7, 32], bioprostheses [84] and smart bandages [102], have been designed. In sports equipments, auxetic foams and textiles have been fabricated to improve impact protection, comfort and flexibility [23]. In structural health monitoring, significant progress has been made by designing smart sensors and actuators exploiting auxeticity [1, 50, 51]. In aircraft industry, auxetic structures have been used for the design of morphing airfoil [34, 10].

Examples of naturally occurring materials with negative Poisson's ratio have recently been discovered, including some classes of crystals [5, 60, 38, 33], biological tissues [100, 52] and blood vessels [97]. However, these natural examples are rare, hence artificially designed geometries leading to auxetic behaviour have been proposed in the literature. The latter are mainly based on the following mechanisms: reentrant structures [48, 18, 57, 9, 73, 115], star-shaped inclusions and pores [96, 66], chirality [74, 85, 37, 93, 9, 2, 71, 68, 89], rotating units [35, 17], pores and cuts [36, 95, 90, 13, 14, 8, 69, 4], instabilities [6, 91, 46], two-dimensional and three-dimensional lattices [11, 12, 16], and other approaches [77, 83, 47, 79, 103, 29, 72].

An alternative idea to create an auxetic medium is to use origami techniques, namely the craft of folding paper. In particular, the Miura-ori pattern is considered here. Named after his inventor, the Japanese astrophysicist Kōryō Miura [65], the Miura-ori folding consists in tessellating a surface by parallelograms, where the latter are rigid so that the deformation is produced by the folding/unfolding

at the creases. Since the tessellation leads to structures with high strength and very low weight, the Miura-ori pattern has been employed in many fields, such as aerospace (e.g., for the deployable structure of satellites), biomedical engineering (e.g., stents) and automotive industry (e.g., airbags) [61]. Recently, Miura-type structures have received many attentions in other areas like aerodynamics [113], stretchable circuit boards [55], conductive elastomers [42] and biosignal recording for health monitoring [41].

Miura-ori tessellations can deform to achieve a desired configuration without yielding. This feature, together with auxeticity and low weight, provides promising potentials for various applications like elastic energy absorption [99] and design of cores of sandwich plates [78, 108]. The mechanical response and energy absorption capabilities of Miura-ori sheet have been investigated in [58] with different experimental tests, i.e. out-of-plane compression, three-point-bending and in-plane compressions along the two principal directions. Design of helmets based on stacked layers of the Miura-Ori folding pattern has also been presented in [39]. Further, the behaviour of Miura-ori patterned metamaterials subjected to dynamic in-plane [45] and out-of-plane [62] compression has been studied by means of numerical and experimental methods. Clearly, the pattern angles as well as the thickness of the facets affect the amount of absorbed energy. For example, in dynamic in-plane problems [45], increasing the angle θ_1 (see Fig. 1) improves the capacity of energy absorbtion. On the other hand, considering out-of-plane compression [62], smaller acute angle of panels is preferable in protection purposes and impact absorbers.

The possibility for an origami pattern to "morph" between a Miura mode and an eggbox mode has allowed for a tunable switch of the Poisson's ratio within a range from negative to positive values [75], and an interesting experimental demonstration involving large deformations and based on a novel Saint-Venant gripping constraint is given in [64]. Origami-inspired metamaterials have also been employed to vary the coefficient of thermal expansion from negative to zero or even positive values [112]. In addition, hydrogenation has been exploited in [63] to transform two-dimensional graphene into three-dimensional graphene origami, whose Poisson's ratio has been determined by means of molecular dynamics simulations and verified by continuum modelling. Metamaterials based on origami patters are characterised not only by auxeticity, but also by bistability and self-locking [110, 44]. Moreover, the composite Miura-ori sheet can be considered as an acoustic metamaterial that possesses both tunable properties (with respect to folding angle) and programmable properties (with respect to geometry of panels) for designing large band, low-frequency acoustic switches [76].

Some methods for manufacturing Miura-ori patterns, such as cold gas-pressure folding for aluminium as the base material, have been introduced in [87]. Based on the multimodal assembly of Miura-Ori tubes and using 3D direct laser writing

3

(DLW), microscale origami metamaterials have been fabricated and their structural response has been characterised using *in situ* scanning electron microscope (SEM) [56]. In that study, kinematic models and nonlinear finite element analysis for auxetic responses and stiffnesses have been employed, as well as Bloch–Floquet finite element analysis for mechanical stability. Studying mechanical response of folded plates as building blocks of many origami/kirigami patterns can pave the way to understanding the behaviour of the entire structure. More recently, vibration characteristics of folded plates have been studied by using the first order shear deformation theory (FSDT) for modelling the facets and use of linear springs for modeling the folds [92].

Finally, it is noted that alternative designs starting from the classical Miura-ori folded structures have been proposed. For instance, a mathematical framework has been introduced in [22] for designing Miura-based cylindrical origami structures with different patterns and cross-sectional shapes, that are foldable and developable. In other studies [80, 81, 82], geometric symmetries of Miura-ori pattern have been developed, and foldability has been investigated. The dislocation of zig-zag strips with resulting introduction of holes has led to lighter systems that are also prone to modifications [26]. Activating predefined creases on curved origami pattern has led to accomplish *in situ* stiffness manipulation covering positive, zero, and negative values [111]. Tunable auxeticity and superflexibility have been obtained in [40] with graphene origami structures. In another study [107], arc-Miura specimens have been manufactured using a stamping process and their mechanical properties under a quasi-static out-of-plane compressive load have been studied, showing that arc-Miura structures have better energy absorption than the corresponding monolithic arches. Weft-knitted Miura-ori folded fabric has been devised to produce three-dimensional structures with negative Poisson's ratio [59]. In addition, two novel origami-based tessellations have been proposed to obtain effective elastic moduli that are larger than those of Miura-ori patterns [105]. Quasi-static and dynamic mechanical properties of graded metamaterials that are made by stacking Miura-ori patterns with different geometric properties have been investigated in order to gain better energy absorption capacity [106]. Programmable properties of origami structures of higher-order elements, made of simple Miura patterns, have also investigated in [43].

In the literature, Miura-ori folded structures have been mainly studied as assemblies of rigid parallelograms that can undergo relative rotations at the creases. Accordingly, the deformation analysis has been performed by means of kinematic considerations together with simple relationships based on the fact that the elasticity of the medium is concentrated on the creases, introducing equivalent discrete springs [88, 104].

Nevertheless, in view of large-scale production, it is of primary interest to

consider folded structures, which do not display neither jumps nor variation of the thickness at the interfaces between different facets and to include their deformation in the homogenisation analysis. This is the main issue that is addressed in this work, where the effective properties of Miura-ori folded structures with different microstructure parameters are evaluated both numerically and experimentally.

In this paper, the unit cells of periodically folded Miura-ori structures are assumed to be elastic, thus they are studied as either plates (where the out-of-plane and the in-plane behaviours are coupled) or solid elements depending on the thickness, which is not assumed to be negligibly small. This allows to create more resistant mechanical systems, whose deformation does not depend only on the geometry, but also on the elastic constants of the material.

The plan of the paper is as follows. In Section 2, the design of the folded structure and the methods to analyse it are described in detail: the geometry of the unit cell is specified in Section 2.1, the periodic and finite systems are presented in Sections 2.2 and 2.3 respectively, and the experimental setup and approach are detailed in Section 2.4. The effective elastic properties of the origami-inspired system are evaluated numerically in Section 3.1, and the numerical results are checked against experimental outcomes in Section 3.2. In Section 4, the results of the work are discussed: in Section 4.1, an overall analysis of the effective mechanical behaviour of the structured medium is carried out based on a thorough parametric analysis, where it is shown that the Poisson's ratio can reach very negative values; in Section 4.2, concluding remarks are provided. Finally, in Appendix A, the negligible effect of out-of-plane displacements on the in-plane auxetic behaviour of the folded structure is demonstrated; in Appendix B, the numerical outcomes of a non-linear analysis are presented and discussed.

2 Design and methods

2.1 Geometry of the unit cell

The elastic system under investigation is based on a Miura-ori folding pattern, consisting of a repetitive arrangement of unit cells, as shown in Fig. 1(a). Each unit cell has uniform thickness t (see part (b)), where t is measured in the direction perpendicular to the facets. The middle surface of the unit cell is made of four identical parallelograms, characterised by the side lengths a and b and the crease angle φ (see part (c)). In the same figure, the folding angle θ_1 and the angles θ_2, η_1 and η_2 are also indicated.

The configuration of the middle surface of the unit cell will be defined by using the parameters a, b, η_1 and η_2. Of course, a different parametrisation can be
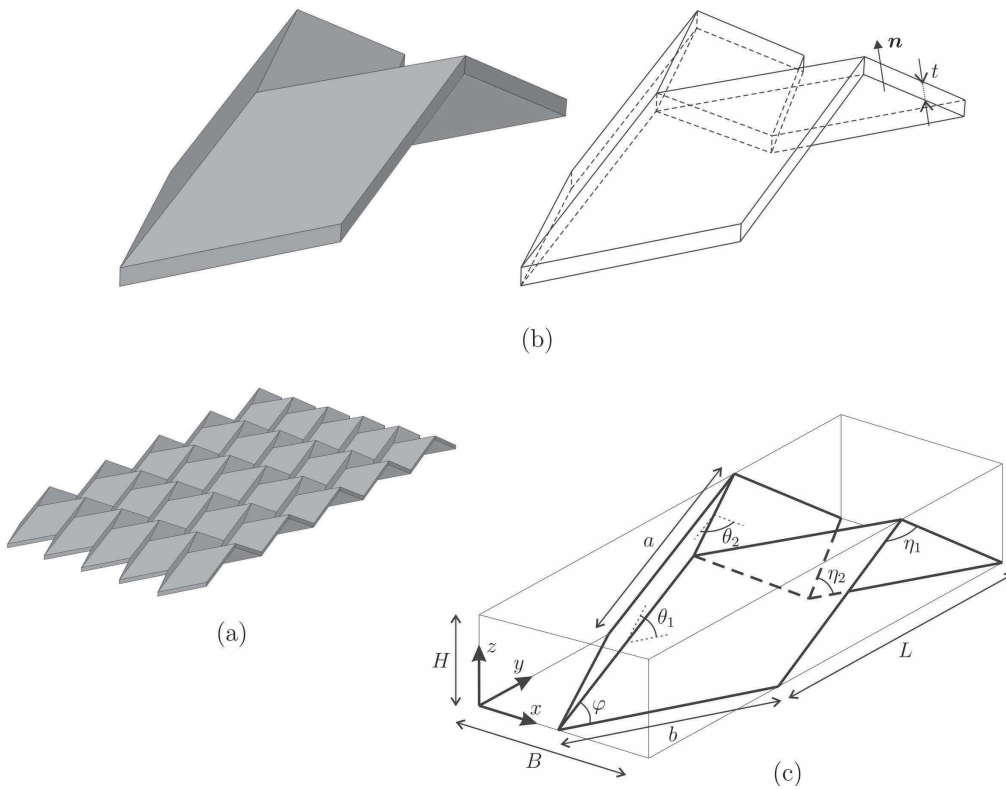
Figure 1: Miura-ori folded structure: (a) system comprising 5×5 unit cells, designed by means of a Miura-ori-like tessellation technique; (b) three-dimensional representation of the unit cell, having uniform thickness t, measured in the direction of the normal $\boldsymbol{n}$ to the facets; (c) geometrical parameters characterising the middle surface of the unit cell. In the figure, $a = b$, $\eta_1 = 125°$ and $\eta_2 = 50°$. The angles φ, θ_1 and θ_2 are defined as functions of η_1 and η_2 in (1).

applied, considering that the following relationships hold:

$$\cos(\varphi) = \sin\left(\frac{\eta_1}{2}\right)\cos\left(\frac{\eta_2}{2}\right), \tag{1a}$$

$$\cos(\theta_1) = \frac{\cos(\eta_1) + \cos(\eta_2)\left[\cos(\eta_1) + 3\right] - 1}{\cos(\eta_1) + \cos(\eta_2)\left[\cos(\eta_1) - 1\right] + 3}, \tag{1b}$$

$$\cos(\theta_2) = \frac{\cos(\eta_2) - \cos(\eta_1)\left[\cos(\eta_2) - 3\right] + 1}{\cos(\eta_1) + \cos(\eta_2)\left[\cos(\eta_1) - 1\right] + 3}. \tag{1c}$$

Vice versa, knowing φ, θ_1 and θ_2, the angles η_1 and η_2 can be calculated from

$$\cos\left(\frac{\eta_1}{2}\right) = \cos\left(\frac{\theta_2}{2}\right)\sin(\varphi), \tag{2a}$$

$$\sin\left(\frac{\eta_2}{2}\right) = \sin\left(\frac{\theta_1}{2}\right)\sin(\varphi). \tag{2b}$$

The dimensions of the unit cell, denoted as L, B and H in Fig. 1(c), are given by

$$L = 2a\sin\left(\frac{\eta_1}{2}\right), \tag{3a}$$

$$B = 2b\sin\left(\frac{\eta_2}{2}\right), \tag{3b}$$

$$H = a\cos\left(\frac{\eta_1}{2}\right), \tag{3c}$$

respectively.

2.2   Periodic model

The unit cell in Figs. 1(b) and 1(c) is built in the finite element package *Comsol Multiphysics* [20] with a continuous three-dimensional model. Standard periodic conditions are imposed at the boundaries of the elementary cell, as discussed in [13, 4]. The mesh consists of tetrahedral elements, whose size is small enough to ensure convergence of the results[1].

The homogenised behaviour of the periodic folded structure is orthotropic, as also verified numerically. Considering also that the interest is in the effective

---

[1]The mesh has been chosen in order to have at least four elements along the thickness, even though convergence could be reached with fewer elements. As an example, for $t = 1$ mm, the mesh assuring convergence of results consists of a total number of degrees of freedom of the order 3.6×10^4. It has also been checked that with a different type of finite elements, namely hexahedral, a mesh with a similar number of degrees of freedom leads to very close results.

behaviour in the $x - y$ plane, the relationship between the reduced strain tensor $\boldsymbol{\epsilon}$ and the reduced stress tensor $\boldsymbol{\sigma}$ can be written in the form

$$\boldsymbol{\epsilon} = \boldsymbol{S}\boldsymbol{\sigma} \implies \begin{pmatrix} \epsilon_{xx} \\ \epsilon_{yy} \\ \epsilon_{xy} \end{pmatrix} = \begin{pmatrix} \frac{1}{E_x} & -\frac{\nu_{yx}}{E_y} & 0 \\ -\frac{\nu_{xy}}{E_x} & \frac{1}{E_y} & 0 \\ 0 & 0 & \frac{1}{2G_{xy}} \end{pmatrix} \begin{pmatrix} \sigma_{xx} \\ \sigma_{yy} \\ \sigma_{xy} \end{pmatrix}, \tag{4}$$

where $\boldsymbol{S}$ denotes the symmetric *compliance matrix*.

The finite element code is capable of providing the *stiffness matrix* $\boldsymbol{C}$, which is the inverse of the compliance matrix:

$$\boldsymbol{C} = \boldsymbol{S}^{-1} = \begin{pmatrix} \frac{E_x}{1-\nu_{xy}\nu_{yx}} & \frac{E_x\nu_{yx}}{1-\nu_{xy}\nu_{yx}} & 0 \\ \frac{E_y\nu_{xy}}{1-\nu_{xy}\nu_{yx}} & \frac{E_y}{1-\nu_{xy}\nu_{yx}} & 0 \\ 0 & 0 & 2G_{xy} \end{pmatrix}. \tag{5}$$

Accordingly, the entries C_{11} and C_{21} represent the macroscopic stress components σ_{xx} and σ_{yy}, respectively, produced by applying a macroscopic strain $\epsilon_{xx} = 1$, and so on.

The terms of $\boldsymbol{C}$ are calculated from the finite element model as follows. Periodic conditions are applied on the boundary faces with normal vectors in the $x-y$ plane, while homogeneous Neumann boundary conditions are imposed on the other faces. The periodic conditions are expressed in terms of kinematic quantities, associated with macroscopic deformations. First, a macroscopic strain ϵ_{xx} is imposed and the corresponding macroscopic stresses are obtained as average over the unit cell of the local stress components; successively, the same procedure is applied to the other two strain components. In this way, the entries in the stiffness matrix $\boldsymbol{C}$ are determined. Then, the effective elastic properties of the structure (namely, E_x, E_y, ν_{xy}, ν_{yx} and G_{xy}) can be easily found by solving an algebraic system of 5 equations using (5).

The thermodynamic limitations for orthotropic media, associated with the positiveness of strain energy, are discussed in [53, 21]. When homogenisation is limited to the $x - y$ plane, the restrictions are simplified as follows:

$$E_x, \, E_y, \, G_{xy} > 0, \tag{6a}$$

$$1 - \nu_{xy}\nu_{yx} > 0, \tag{6b}$$

$$|\nu_{yx}| < \sqrt{\frac{E_y}{E_x}}, \tag{6c}$$

$$|\nu_{xy}| < \sqrt{\frac{E_x}{E_y}}. \tag{6d}$$

2.3 Finite structure

An alternative approach consists in examining the finite system, shown in Fig. 2(a), which is intended to reproduce the real specimen, described in Section 2.4.1. The folded part of the structure comprises 9×11 unit cells.

The structure in Fig. 2(a) is modelled with a finite element code, developed in *Comsol Multiphysics*. On the bottom surface, parallel to the xz-plane, the displacements are prevented; conversely, a uniform displacement along the y-axis, denoted as v_0, is applied on the top surface parallel to the xz-plane.

The Poisson's ratio is evaluated by calculating the displacements at the points A to D in Fig. 2(a), that are located in a central region to avoid boundary effects. More specifically, $\nu_{yx} = -\epsilon_{xx}/\epsilon_{yy}$, where $\epsilon_{xx} = (u_\text{B} - u_\text{A})/(x_\text{B} - x_\text{A})$ and $\epsilon_{yy} = (v_\text{D} - v_\text{C})/(y_\text{D} - y_\text{C})$.

2.4 Experimental validation

In order to demonstrate the validity of the numerical methods described in the previous sections, an extensive experimental campaign has been carried out, where specimens of different materials and geometries have been produced and tested in the Experimental Mechanics Laboratory of the University of Cagliari.

2.4.1 Specimen design and production

The specimen consists of a matrix of 9×11 Miura-ori cells, as illustrated in Fig. 2(b). In order to avoid boundary effects, the measurements are taken in the central region of the specimen. The edges perpendicular to the loading direction are designed to grip the specimen in an easier and repeatable way, especially in terms of alignment.

The materials used in the first campaign of tests are polymers such as PLA (Polylactic Acid) and ABS (Acrylonitrile Butadiene Styrene); in this perspective, it is observed that it is of great importance to make the gripped zone stiffer than the core itself, because excessive pressure exerted by grips may cause large localised deformations or even failure before the test starts. In order to overcome this problem, M6 nuts are inserted to better distribute the applied load and, hence, reduce stress concentration; since they are stiffer than the polymers, the M6 nuts preserve the structural integrity of the specimen in the gripped zone.

The Miura-ori geometry is known to have amazing advantages in terms of mechanical response [88], but it conceals significant manufacturing problems. This kind of issue is due to the geometry itself: using conventional milling appears ineffective because it is impossible to preserve the cell's sharp edges, since the mill has a non-zero fillet radius. The tool length is another critical parameter in
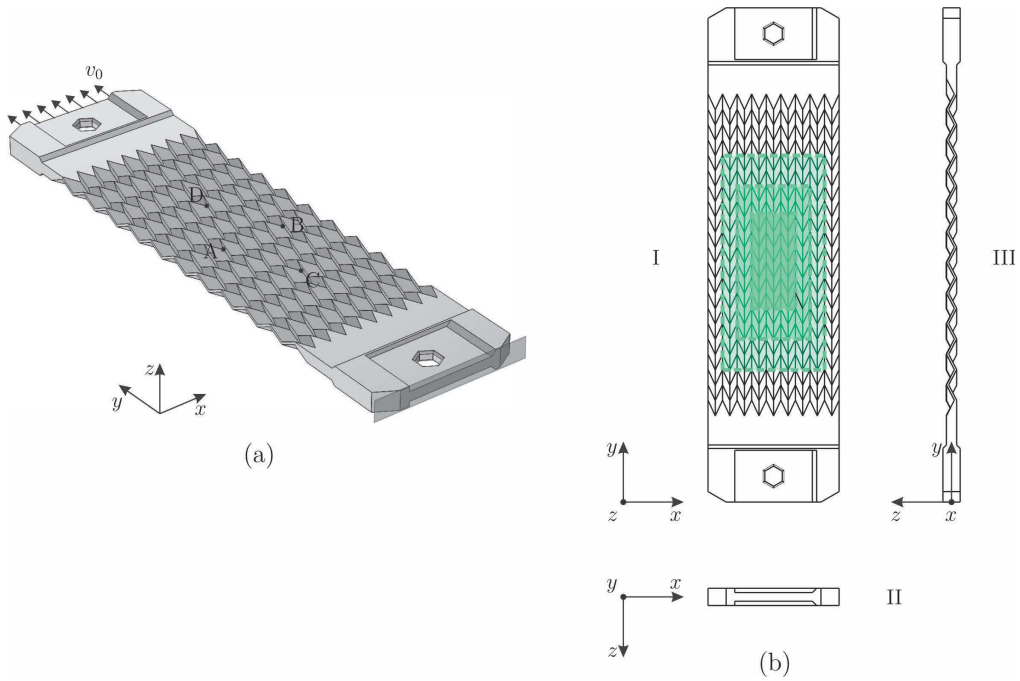
Figure 2: (a) Finite structure containing a tessellation of unit cells as in Fig. 1, subjected to a uniform displacement along the y-axis (and null displacements in the two perpendicular directions) at the top surface and constrained in all directions at the bottom surface. (b) Specimen's geometry used in experimental tests: (I) top, (II) front and (III) lateral view; the values of Poisson's ratio are evaluated experimentally from the average deformation components, measured in different areas of the specimen (some representative regions are shown here).

this kind of process, so the conventional cutting technologies must be avoided. Several manufacturing techniques were proposed in the literature, among which the so-called "*Cold Gas-Pressure Folding*", developed in [87], represents one of the most advanced methods. In this article 3D printing technology, in particular the FFF (Fused Filament Fabrication), has been used to manufacture models based on Miura-ori folding pattern. This technique, also employed in [101], appears to be suitable since it preserves all the specifications of Miura-ori geometry. In particular, the edges are sharp and the thickness is uniform, with no over-deposit of fused material. The printer is a Prusa i3 MK2, characterised by a Cartesian kinematic scheme (see Fig. 3(a)).

2.4.2 Experimental setup

The experimental setup consists of a servo-hydraulic multi-purpose MTS Landmark 370 test machine (see Fig. 3(b)), equipped with a load cell having a range of $\pm 100 \, \text{kN}$ and a hydraulic actuator with the same load capacity. The tests have been conducted in a displacement-controlled way. An image is acquired at each displacement step, in order to use the Digital Image Correlation (DIC) technique (described below). The camera is a monochromatic Allied Vision Pike F341b, equipped with a Schneider Makro lens to ensure a global vision of the specimen. The experimental apparatus employed to perform the tensile test on the specimen and the measurement devices are illustrated in Fig. 3(c).

The first experimental campaign consists of nine specimens of different thickness, five of which are made of PLA while the remaining four are obtained from ABS filaments. The Poisson's ratio of both these materials, that has been obtained experimentally by means of a classical traction test, is equal to 0.35. It is also pointed out that the thickness is measured perpendicularly between the two faces of a facet, as in Fig. 1(b).

The acquired images have been processed with an in-house software for DIC analysis. DIC is an optical technique, whose main goal is the identification of the displacement field between a reference image (e.g., at rest) and a target one after motion [94]. First, the specimen surface is treated with an isotropic pattern (e.g, sprayed with an aerograph). Then, the image is partitioned in small areas, named subsets, and DIC aims to find the displacement of each subset in the target image [94]. The key assumption is that the pixel intensity never changes during motion, namely, the optical flow remain constant through the test (this requirement is never fully satisfied because of several noise sources, but the change of intensity is negligibly small for the purpose of the current experimental campaign). Figure 3(d) highlights the uniform enlightenment of the specimen provided by the lamp.

The entire Region of Interest (ROI) is partitioned into a mesh, in which the

Figure 3: (a) 3D printer used in the production of the specimens, one of which is shown in the picture; (b) Universal Test Machine MTS Landmark 370; (c) experimental apparatus with measurement devices; (d) specimen uniformly enlightened by the lamp, with details of the gripping system.

displacement field inside each element is controlled by nodal parameters [3]. This method gives several advantages in terms of displacement standard deviation reduction [3].

The Poisson's ratio is estimated as the (negative) ratio between the transverse and the longitudinal engineering strains. The latter have been calculated from the displacements measured in different regions, some of which are indicated with different green hues in Fig. 2(b). Further, the Poisson's ratios at different loading steps have been computed. Then, the averages and standard deviations of ν_{yx} have been determined referring to the whole set of data for all the considered regions and for all the loading steps within the elastic range.

3 Results

3.1 Numerical determination of the effective elastic properties

In this section, it is demonstrated that the elastic structure in Fig. 1(a) is auxetic in the xy-plane by showing that the Poisson's ratio ν_{yx} is negative. The latter is calculated for both the periodic and finite structures, presented in Sections 2.2 and 2.3, respectively.

It is assumed that the material composing the folded structure is isotropic, with Young's modulus $E_m = 3035$ MPa and Poisson's ratio $\nu_m = 0.35$. These values correspond to the elastic constants of PLA (Polylactic Acid), used to produce the specimens described in Section 2.4.1. The geometrical parameters of the unit cell are taken as $a = b = 10$ mm, $\eta_1 = 125°$ and $\eta_2 = 50°$.

3.1.1 Periodic model

Different values for the thickness t are considered, within the range $(0, 10]$ mm. The results of the periodic analysis are reported in Fig. 4 by a black solid line. It is apparent that the Poisson's ratio ν_{yx} is a monotonically increasing function of the thickness. Furthermore, for sufficiently low values of the thickness $\nu_{yx} < 0$, hence the structure expands in the x-direction when stretched in the y-direction (see also Fig. 1).

When the thickness tends to zero, three-dimensional brick elements cannot be used to create the mesh, but shells are preferable to model the facets of the unit cell[2]. Following a procedure similar to that outlined in Section 2.2, the grey solid

---

[2]The chosen mesh of the shell model, consisting of triangular elements, is characterised by around 1.0×10^4 degrees of freedom.
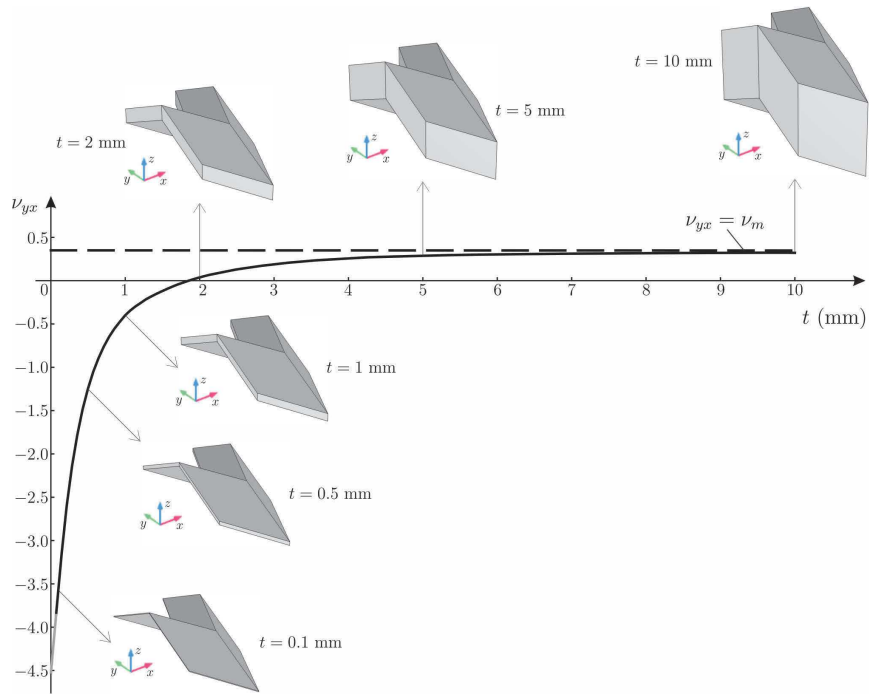
Figure 4: Effective Poisson's ratio ν_{yx} versus the thickness t (black solid line), calculated for $a = b = 10$ mm, $\eta_1 = 125°$ and $\eta_2 = 50°$. The black dashed line indicates the limit of ν_{yx} for large values of the thickness; this limit coincides with the Poisson's ratio of the material. The grey solid line is obtained with a shell model. In the insets, illustrations of the periodic cell for different values of the thickness t are presented.

curve in Fig. 4 is determined employing shell elements. It is noted that when $t \to 0$ the Poisson's ratio approaches a finite value, equal to -4.4, that corresponds to the value predicted by the Miura-ori sheets [88], as explained in more detail in Section 4. On the other hand, for large values of the thickness ν_{yx} tends to the Poisson's ratio of the material ν_m, as expected.

3.1.2 Finite structure

The deformed shape of the finite system in the xy-plane, computed for a thickness equal to $t = 0.85$ mm and an imposed displacement $v_0 = 10$ mm, is illustrated in Figs. 5(a) and 5(b). The deformed configuration clearly shows that the system is auxetic. In part (a), the displacement component v in the y-direction is presented; it is evident that v increases linearly along the positive y-axis. In part (b), the displacement component u in the x-direction is symmetric with respect to the central line of the model parallel to the y-axis. It is important to underline that the model deforms exhibiting displacements also in the z-direction; nevertheless, the presence of out-of-plane displacements does not alter the in-plane behaviour of the system (see Appendix A).

The comparative analysis between the numerical results of the unit cell and the finite specimen shows that, for a thickness $t = 0.85$ mm, the finite model yields $\nu_{yx} = -0.53$, while the periodic analysis provides $\nu_{yx} = -0.55$. For $t = 1.70$ mm, the Poisson's ratios of the finite structure and of the periodic system are instead given by $\nu_{yx} = 0.01$ and $\nu_{yx} = -0.03$, respectively. After checking for other values of the thickness, which are not given here for brevity, it is concluded that the agreement between the finite and the periodic systems is satisfactorily good.

The periodic analysis will also be employed in the discussion in Section 4.1 to investigate the effect of different parameters on the effective Poisson's ratio of the folded structure.

3.2 Experimental results

The cells of the specimens have the same dimensions as those considered in Section 3.1, namely $a = b = 10$ mm, $\eta_1 = 125°$ and $\eta_2 = 50°$ (see Fig. 1(c)).

Figure 6 includes all the results obtained from the experimental tests. The black and blued dots indicate the values of the effective Poisson's ratio for PLA and ABS specimens, respectively. The data corresponding to PLA and ABS show a similar tendency as the thickness is varied.

On the other hand, the black solid line in Fig. 6 indicates the numerical results, computed from the periodic analysis. The comparison between the experimental and numerical findings shows that the experimental points are very close to the
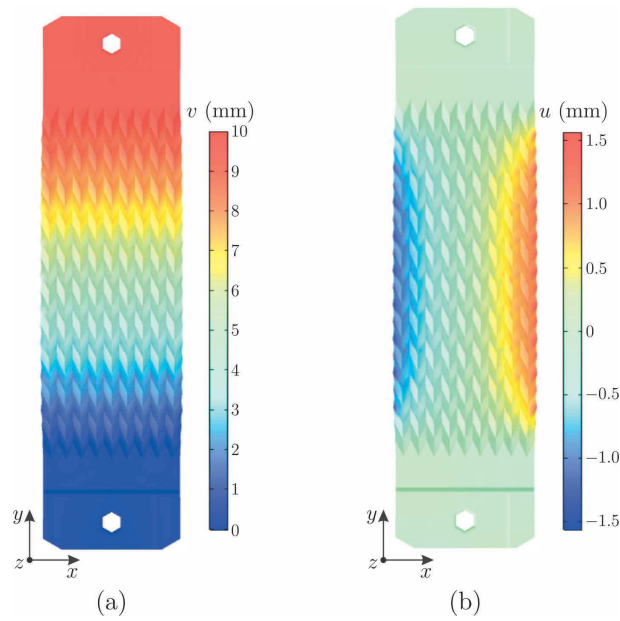
Figure 5: Colour maps of the displacement component along the (a) y-direction and (b) x-direction. The points where the displacements are calculated for the evaluation of the Poisson's ratio are highlighted in Fig. 2(a). In the simulations, $a = b = 10$ mm, $t = 0.85$ mm, $\eta_1 = 125°$, $\eta_2 = 50°$ and $v_0 = 10$ mm (refer to Fig. 2(a)).

16

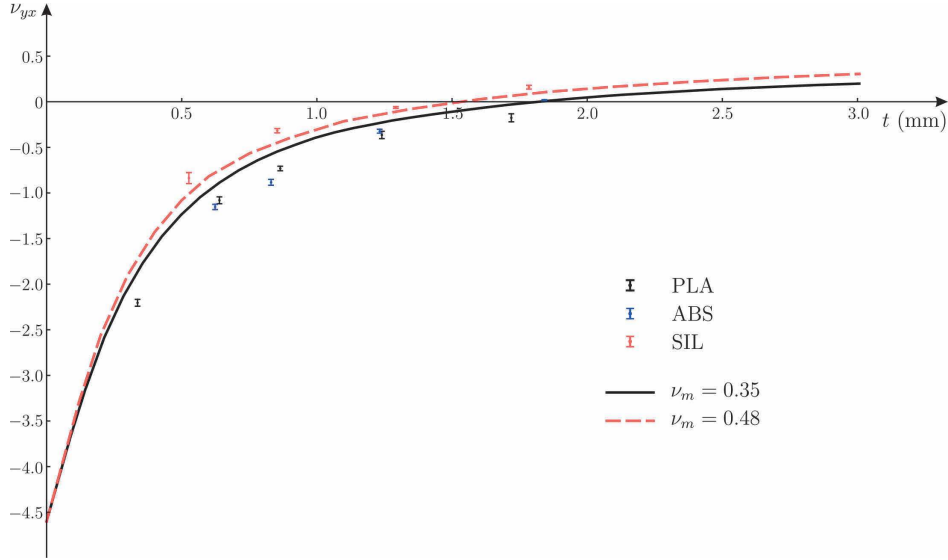Figure 6: Comparison between experimental outcomes (dots with error bars) and numerical results (lines). The geometrical parameters of the microstructure are identical to those considered in Fig. 4.

curve determined numerically and follow a similar trend. Nonetheless, the experimental data lie below the curve. This can be explained by considering that the FFF technology is based on filament deposition, so it introduces a certain degree of anisotropy that is difficult to model in the numerical computations.

The anisotropy issue can be resolved by using a different technique to fabricate the specimens. Accordingly, in a second experimental campaign, a set of silicon specimens have been produced using a mold, that is designed according to the actual specimen's geometry. The silicon is a fluid rubber, that has been poured in the mold and then cured to obtain the desired mechanical and geometrical properties. The values of the effective Poisson's ratio of the silicon specimens for four different thicknesses are reported in Fig. 6, where they are represented by red dots.

The Poisson's ratio of silicon is 0.48. Accordingly, the experimental outcomes are compared with the red dashed line shown in Fig. 6, that is calculated numerically by taking $\nu_m = 0.48$. In this case, the comparison between the experimental and numerical results shows an even better agreement, removing the unknown effect of the anisotropy introduced by FFF technique.

The results of the DIC analysis obtained for an ABS specimen having thickness $t = 0.83$ mm are shown in Fig. 7. In particular, parts (a) and (b) present the fields
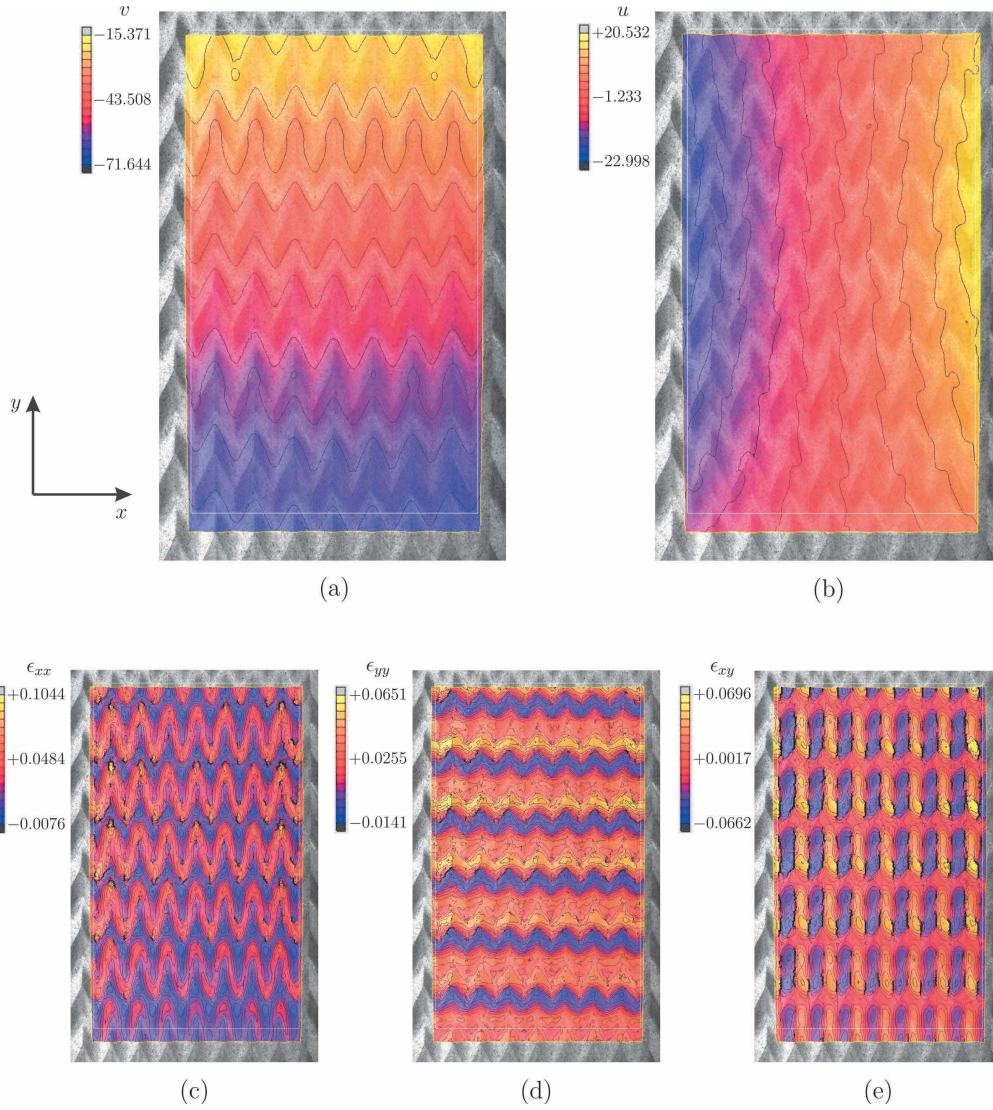
17

Figure 7: Results of DIC post-processing for an ABS specimen with $t = 0.83$ mm: (a) displacement component v in the y-direction; (b) displacement component u in the x-direction; small deformation components (c) ϵ_{xx}, (d) ϵ_{yy} and (e) ϵ_{xy}. The values of the displacement components in the legends are given in pixels.

of the displacement components v and u, respectively, which clearly emphasise the auxetic behaviour of the Miura-ori model. Conversely, parts (c) and (d) show the small deformation fields ϵ_{xx} and ϵ_{yy}, while part (e) illustrates the distribution of the ϵ_{xy} component of the strain tensor. The deformation fields further prove that the effective Poisson's ratio ν_{yx} is negative, since the average values of both the strain components ϵ_{xx} and ϵ_{yy} are clearly positive. In addition, the similarity of the field distribution in each cell and the effect of the boundary conditions on the finite specimen can be noted.

In the video included in the Supplementary Material, the same ABS specimen with thickness $t = 0.83$ mm is considered. The auxetic behaviour of the folded structure is clearly shown in the left part of the video. On the right, the diagrams of the measured load (top) and Poisson's ratio (bottom) versus the imposed displacement at each step are presented. From these diagrams, it is apparent that, after an initial settlement, the specimen behaves as a linear elastic material, characterised by a linear relationship between the load and the displacement (top) and a constant value of the Poisson's ratio (bottom). Beyond the linear range, the structure starts undergoing large and subsequently anelastic deformations, which have not been considered in the present work for the evaluation of the effective Poisson's ratio and are left for future investigations.

4 Discussion

4.1 Parametric study

The aim of this section is to discuss how the effective properties of the Miura-ori structure change as the microstructural parameters η_1 and η_2, characterising its microgeometry (see Fig. 1(c)), are varied. For this purpose, numerical simulations are performed in *Comsol Multiphysics*, using the unit cell in Figs. 1(b) and 1(c) with periodic conditions imposed on the boundaries.

In the computations, the size of the projection of the periodic cell on the xy-plane is kept constant and equal to $[B = 4$ mm$] \times [L + b\cos(\eta_2/2) = 10$ mm$]$. As in Section 3, the material is assumed to be isotropic, having Young's modulus $E_m = 3035$ MPa and Poisson's ratio $\nu_m = 0.35$. Accordingly, the shear modulus of the material is given by $G_m = E_m/[2(1 + \nu_m)] = 1124$ MPa.

In the diagrams presented in the following, the dotted lines indicate the results provided by the shell model (used when the thickness is in the interval $[10^{-6}, 0.1]$ mm), while the continuous lines are obtained with the solid model. Hence, a small discrepancy is generally observed for $t = 0.1$ mm. Effective properties have been evaluated for $t/B \in (0, 0.75]$, which has been considered as the interval of interest for technological applications.

19

In the simulations, the trends of the effective Poisson's ratios ν_{yx} and ν_{xy} for varying thickness t and angle η_1 are analysed. The graphs representing these two effective parameters are plotted in Figs. 8(a) and 8(b), respectively, taking a fixed value of $\eta_2 = 50°$. It is evident that $\nu_{yx} < 0$ when the thickness is sufficiently small, implying that the Miura-ori folded structure is auxetic. For very thin models ($t \to 0$), the Poisson's ratio ν_{yx} is much smaller than -1, so that the effective orthotropic materials display lateral expansions several times larger than the applied longitudinal extensions.

For any value of η_1 considered in Fig. 8(a), ν_{yx} increases monotonically with t. Moreover, for a fixed value of the thickness, ν_{yx} increases (i.e. decreases in amplitude in the auxetic region) as the angle η_1 is increased. For every curve, the minimum value of ν_{yx} is attained in the limit when $t \to 0$. On the other hand, the effective Poisson's ratio ν_{xy} exhibits a minimum for a finite positive value of the thickness t. In such a case, the thickness t corresponding to the minimum depends on the angle η_1, while its minimum values remain in the range $\nu_{xy} \in (-0.26, -0.25)$.

Comparing Figs. 8(a) and 8(b), it is apparent that the considered medium is anisotropic and its auxeticity is more remarkable when the structure is stretched in the y-direction than in the x-direction, since $|\nu_{yx}| > |\nu_{xy}|$ in the range of thicknesses where the medium is auxetic.

In Fig. 8(c), the values of the thickness for which the Miura-ori folded structure is characterised by null Poisson's ratios are reported as functions of angle η_1. Of course, the diagram is a monotonically decreasing function of η_1, as can also be inferred from Figs. 8(a) and 8(b).

It is also interesting to note that, when the thickness tends to zero, the structure behaves like a Miura-ori sheet, whose Poisson's ratio can be determined only kinematically. In particular, ν_{yx} can be calculated as [88] [3]

$$\nu_{yx} = \frac{1}{\nu_{xy}} = -\frac{1}{[\tan(\eta_2/2)]^2} \,. \tag{7}$$

The formula above is verified by the independent numerical results reported in Figs. 8(a) and 8(b), where, in this limit $t \to 0$, $\nu_{yx} \to -4.599$ and $\nu_{xy} = \nu_{yx}^{-1} \to -0.2174$ independently of the value of η_1.

In order to fully evaluate the behaviour of the folded structure in the xy-plane, the effective Young's moduli E_x and E_y and the effective shear modulus G_{xy} are presented in Figs. 9(a), 9(b) and 9(c), respectively. All these properties are monotonically increasing functions of the thickness. Young's moduli E_x and E_y tend to zero as $t \to 0$, while the curves corresponding to the shear modulus have finite values, depending on η_1, in this limit. This is expected on physical

---

[3]Note that γ, θ and ν_{SL} in [88] correspond to φ, $(\pi - \theta_2)/2$ and ν_{xy} in this paper.
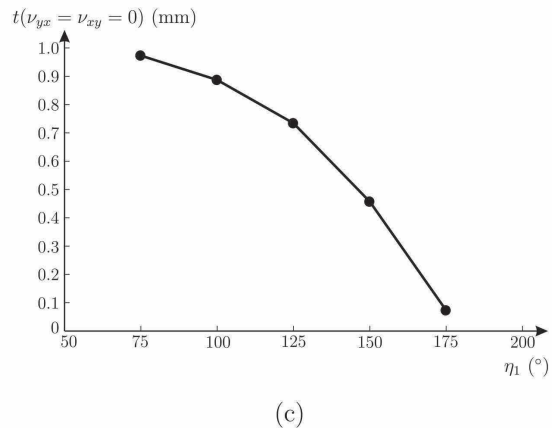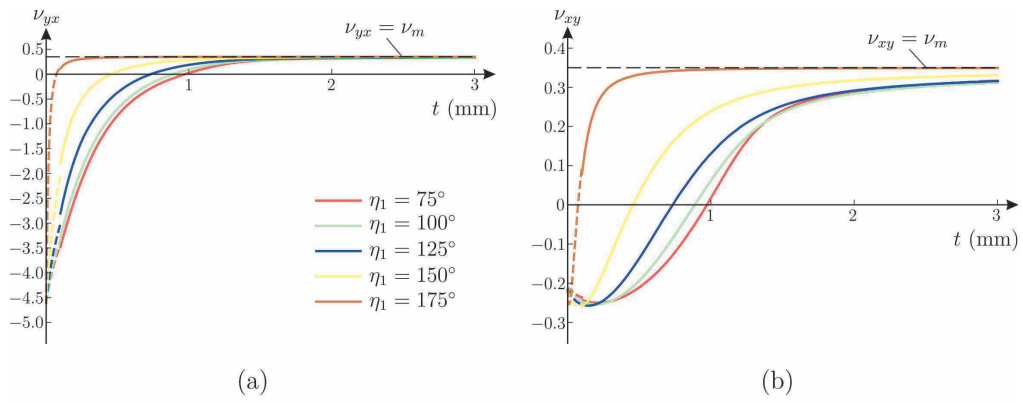
Figure 8: Effective Poisson's ratios ν_{yx} (a) and ν_{xy} (b) as functions of thickness t and for different values of angle η_1. (c) Values of the thickness t for which $\nu_{yx} = \nu_{xy} = 0$ for different values of η_1. In these simulations, angle $\eta_2 = 50°$.
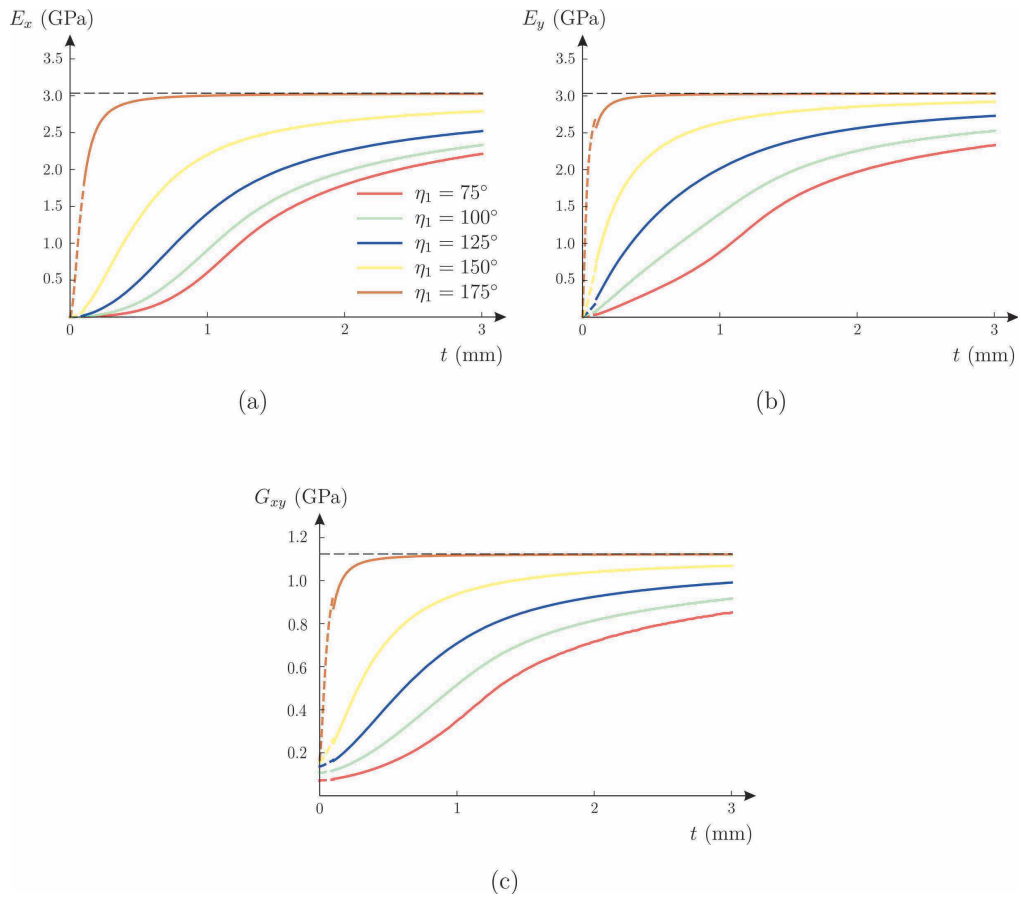
Figure 9: Effective Young's moduli E_x (a) and E_y (b) and effective shear modulus G_{xy} (c) versus thickness t, computed for different values of angle η_1. In these simulations, angle $\eta_2 = 50°$.
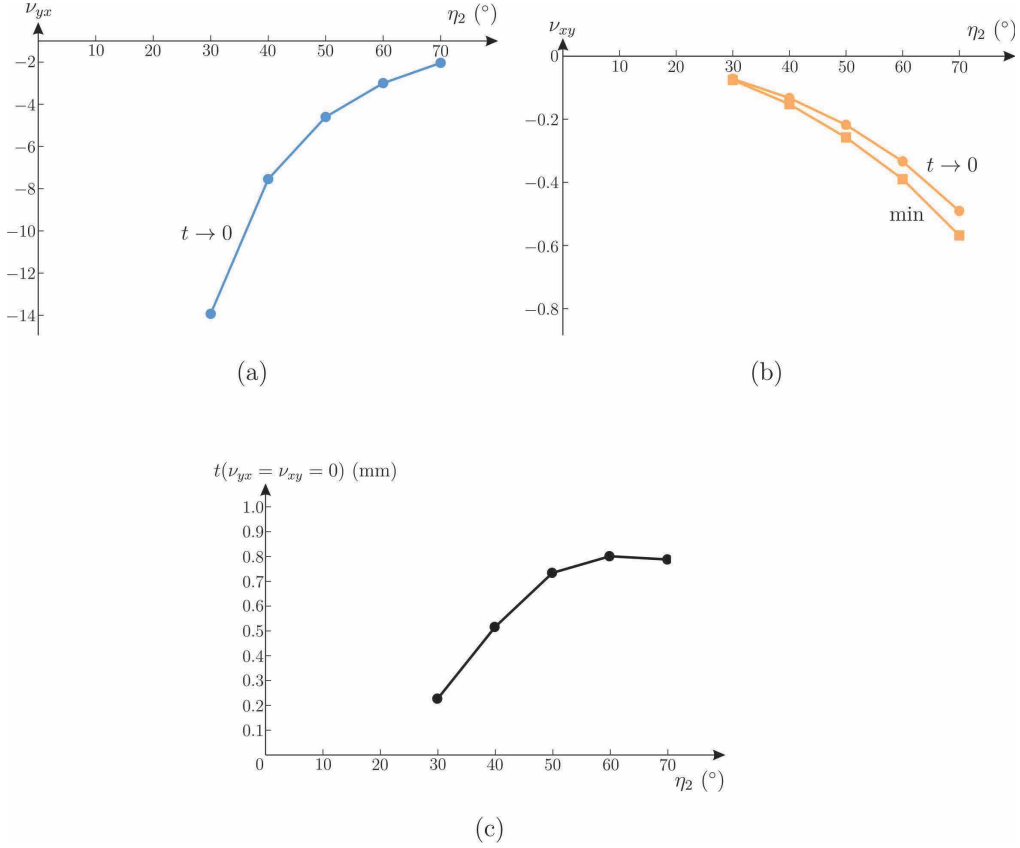
22

Figure 10: Effective Poisson's ratios ν_{yx} (a) and ν_{xy} (b) as functions of the angle η_2, when $t \to 0$. The minimum of ν_{xy} is also given in part (b). (c) Values of the thickness t for which $\nu_{yx} = \nu_{xy} = 0$ for different values of η_2. In these simulations, angle $\eta_1 = 125°$.

grounds, since a Miura-ori sheet (having $t \to 0$) can be stretched longitudinally without a significant effort, while it provides resistance to in-plane shear loading or deformation. In addition, for a given value of t, E_x, E_y and G_{xy} increase by increasing angle η_1. Obviously, for large values of the thickness, the effective elastic moduli tend to the values of the elastic constants of the material E_m and G_m, indicated by the horizontal dashed lines in the figures, where isotropy is also recovered.

For all values of the parameters, the thermodynamic limitations (6) are always satisfied. In particular, from Fig. 9 it is apparent that the effective elastic moduli are all positive. Further, from Fig. 8 it is possible to infer that $1 - \nu_{xy}\nu_{yx}$ is always positive and tends to zero in the limit when $t \to 0$ (see also (7)).

The effective behaviour as a function of the angle η_2, not reported here for brevity, gives the same qualitative results as in Figs. 8 and 9, with one important difference. In analogy with the previous study, ν_{yx}, E_x, E_y, and G_{xy} are monotonically increasing functions of the thickness t, while ν_{xy} has a minimum at a finite value of the thickness $t \simeq 0.1$ mm; for $t \to 0$ and $t \to \infty$ the effective behaviour tends to the Miura-ori sheet and to the isotropic material one, respectively. However, when $t \to 0$ the Poisson's ratios ν_{yx} and ν_{xy} do not tend to constant values, but to limits that depend on the angle η_2, as in Eq. (7) and consistently with the findings of [88]. These limits are reported in Figs. 10(a) and 10(b), where the minima of ν_{xy} are also given. Once again, it is verified in Fig. 10 that $|\nu_{yx}| > |\nu_{xy}|$. The values of t for which the Poisson's ratios are equal to zero are given in Fig. 10(c) for different values of angle η_2.

4.2 Concluding remarks

In this paper, the static behaviour of a Miura-ori folded structure has been investigated, with special attention on the negative Poisson's ratios exhibited by the orthotropic medium. Differently from previous studies [88], the thickness of the facets can have either small or significantly large values. Consequently, the system's unit cells have been studied as shell or solid elements, depending on the value of the thickness. Such analysis includes the contribution of the deformation of the folded plates, the interaction between the in-plane and out-of-plane responses of the facets, together with the evaluation of the mechanical behaviour of the connecting edge regions between folded plates, for which a full three-dimensional analysis with solid elements is needed to give accurate results.

When the Miura-ori structure is subjected to a uniaxial tensile load, two competing mechanisms are activated. The first one is based on the rigid rotations of the facets, while the other one on the lateral contraction of the material (considering that the latter has positive Poisson's ratio). For small values of the thickness, the first mechanism is predominant. As the thickness is increased, the mechanism associated with rigid rotations tends to diminish with a trend that is faster than linear reduction.

One of the targets of the study is to give an insight on the mechanical properties of microstructures which are prone to large-scale industrial production, and the possibility to choose a considerable value for the thickness allows to employ the proposed structure in engineering applications, where the load-carrying capacity is an essential requirement.

The effective properties of the Miura-ori sheet have been determined both numerically and experimentally. First, periodic analysis has been used to calculate the homogenised Poisson's ratios and elastic moduli of the system. Successively, a

finite Miura-ori structure has been modelled with a finite element code, validating the results obtained from the periodic structure. Specimens of different materials and geometries have also been fabricated and tested, and the comparison between the experimental findings (determined by means of the Digital Image Correlation technique) and the numerical outcomes has shown a good agreement. Finally, a parametric analysis has been performed to assess the effect of different geometrical quantities on the effective properties of the auxetic medium. The limiting values for Miura-ori sheet and for the folded structure with large thickness are retrieved and, for the geometrical parameters considered in the present study, $|\nu_{yx}| > |\nu_{xy}|$, differently from [88]. The study indicates that the amplitude of ν_{yx} decreases with t in the auxetic region, while it is possible to find an optimal thickness ($t \simeq 0.1$ mm) that minimizes ν_{xy}.

The nonlinear analysis is left for future work, since the regime where considerable geometrical nonlinearities are present overlaps the regime where significant damage develops due to the stress concentration at the edge interfaces between the folded plates. In such a case, an accurate study accounting for material and structural responses deriving from the technology implemented for the production of the specimens must be considered. Some preliminary results for a hyper-elastic material with geometrical non-linearities are presented in Appendix B.

It is expected that this model can have important applications in different fields, such as aerospace, biomedical, civil and mechanical engineering.

References

[1] Alderson A, Alderson KL. 2007. Auxetic materials. *Proc. Inst. Mech. Eng. G* **221**, 565–575.

[2] Bacigalupo A, Gambarotta L. 2020. Chiral two-dimensional periodic blocky materials with elastic interfaces: Auxetic and acoustic properties. *Extreme Mech. Lett.* **39**, 100769.

[3] Baldi A, Bertolino F. 2016. Assessment of h-refinement procedure for global digital image correlation. *Meccanica* **51**, 979–991.

[4] Baldi A, Brun M, Carta G. 2022. Three-dimensional auxetic porous medium. *Mech. Mater.* **164**, 104114.

[5] Baughman RH, Shacklette JM, Zakhidov AA, Stafström S. 1998. Negative Poisson's ratio as a common feature of cubic metals. *Nature* **392**, 362–365.

[6] Bertoldi K, Reis PM, Willshaw S, Mullin T. 2010. Negative Poisson's ratio behavior induced by an elastic instability. *Adv. Mater.* **22**(3), 361–366.

[7] Bhullar SK, Ko J, Ahmed F, Jun MBG. 2014. Design and fabrication of stent with negative Poisson's ratio. *Int. J. Mech. Aerosp. Ind. Mechatron. Eng.* **8**, 462–468.

[8] Box F, Johnson CG, Pihler-Puzović D. 2020. Hard auxetic metamaterials. *Extreme Mech. Lett.* **40**, 100980.

[9] Bruggi M, Corigliano A. 2019. Optimal 2D auxetic micro-structures with band gap. *Meccanica* **54**, 2001–2027.

[10] Budarapu PR, Sudhir Sastry YB, Natarajan R. 2016. Design concepts of an aircraft wing: composite and morphing airfoil with auxetic structures. *Front. Struct. Civ. Eng.* **10**(4), 394–408.

[11] Cabras L, Brun M. 2014. Auxetic two-dimensional lattices with Poisson's ratio arbitrarily close to -1. *Proc. R. Soc. Lond. A* **470**(2172), 20140538.

[12] Cabras L, Brun M. 2016. A class of auxetic three-dimensional lattices. *J. Mech. Phys. Solids* **91**, 56–72.

[13] Carta G, Brun M, Baldi A. 2016. Design of a porous material with isotropic negative Poisson's ratio. *Mech. Mater.* **97**, 67–75.

[14] Carta G, Cabras L, Brun M. 2016. Continuous and discrete microstructured materials with null Poisson's ratio. *J. Eur. Ceram. Soc.* **36**(9), 2183–2192.

[15] Chan N, Evans KE. 1998. Indentation resilience of conventional and auxetic foams. *J. Cell. Plast.* **34**, 231–260.

[16] Chen X, Moughames J, Li Q, Martínez JAI, Tan H, Adrar S, Laforge N, Cote J-M, Euphrasie S, Ulliac G, Kadic M, Laude V. 2020. Optimal isotropic, reusable truss lattice material with near-zero Poisson's ratio. *Extreme Mech. Lett.* **41**, 101048.

[17] Chetcuti E, Ellul N, Manicaro E, Brincat J, Attard D, Gatt R, Grima J. 2014. Modeling auxetic foams through semi-rigid rotating triangles. *Phys. Status Solidi b* **251**(2), 297–306.

[18] Choi JB, Lakes RS. 1992. Non-linear properties of polymer cellular materials with a negative Poisson's ratio. *J. Mater. Sci.* **27**(17), 4678–4684.

[19] Choi JB, Lakes RS. 1996. Fracture toughness of re-entrant foam materials with a negative Poisson's ratio: experiment and analysis. *Int. J. Fract.* **80**, 73–83.

[20] COMSOL Multiphysics®v. 5.5. www.comsol.com. COMSOL AB, Stockholm, Sweden.

[21] Cowin SC, Van Buskirk WC. 1986. Thermodynamic restrictions on the elastic constants of bone. *J. Biomechanics* **19**(1), 85–87.

[22] Du Y, Keller T, Song C, Xiao Z, Wu L, Xiong J. 2021. Design and foldability of Miura-based cylindrical origami structures. *Thin-Walled Struct.* **159**, 107311.

[23] Duncan O, Shepherd T, Moroney C, Foster L, Venkatraman PD, Winwood K, Allen T, Alderson A. 2018. Review of auxetic materials for sports applications: Expanding options in comfort and protection. *Appl. Sci.* **8**, 941.

[24] Easey N, Chuprynyuk D, Syazwan Wan Musa WM, Bangs A, Dobah Y, Shterenlikht A, Scarpa F. 2019. Dome-shape auxetic cellular metamaterials: Manufacturing, modeling, and testing. *Front. Mater.* **6**, 86.

[25] Eghbali P, Younesian D, Farhangdoust S. 2020. Enhancement of the low-frequency acoustic energy harvesting with auxetic resonators. *Appl. Energy* **270**, 115217.

[26] Eidini M. 2016. Zigzag-base folded sheet cellular mechanical metamaterials. *Extreme Mech. Lett.* **6**, 96–102.

[27] Evans KE. 1991. Auxetic polymers: a new range of materials. *Endeavour* **15**(4), 170–174.

[28] Evans KE, Alderson KL. 2000. Auxetic materials: the positive side of being negative. *Eng. Sci. Educ. J.* **9**(4), 148–154.

[29] Farrugia P-S, Gatt R, Mizzi L, Grima JN. 2021. Auxetic behavior obtained through the large deformations of variants of the rectangular grid. *Mech. Adv. Mat. Struct.*, 1–10.

[30] Francesconi L, Baldi A, Dominguez G, Taylor M. 2020. An investigation of the enhanced fatigue performance of low-porosity auxetic metamaterials. *Exp. Mech.* **97**, 93–107.

[31] Francesconi L, Baldi A, Liang X, Aymerich F, Taylor M. 2019. Variable Poisson's ratio materials for globally stable static and dynamic compression resistance. *Extreme Mech. Lett* **26**, 1–7.

[32] Gatt R, Mizzi L, Azzopardi JI, Azzopardi KM, Attard D, Casha A, Briffa J, Grima JN. 2015. Hierarchical auxetic mechanical metamaterials. *Sci. Rep.* **5**, 8395.

[33] Goldstein RV, Gorodtsov VA, Lisovenko DS. 2010. Auxetic mechanics of crystalline materials. *Mech. Solids* **45**, 529–545.

[34] Gong X, Huang J, Scarpa F, Liu Y, Leng J. 2015. Zero Poisson's ratio cellular structure for two-dimensional morphing applications. *Compos. Struct.* **134**, 384–392.

[35] Grima JN, Alderson A, Evans KE. 2005. Auxetic behaviour from rotating rigid units. *Phys. Status Solidi b* **242**(3),561–575.

[36] Grima JN, Gatt R. 2010. Perforated sheets exhibiting negative Poisson's ratios. *Adv. Eng. Mater.* **12**(6), 460–464.

[37] Grima JN, Gatt R, Farrugia PS. 2008. On the properties of auxetic meta-tetrachiral structures. *Phys. Status Solidi b* **245**(3), 511–520.

[38] Grima JN, Jackson R, Alderson A, Evans K. 2000. Do zeolites have negative Poisson's ratios? *Adv. Mater.* **12**(24), 1912–1918.

[39] Hanna B. 2020. *Development of a Metamaterial for use in American Football Head Protection*. PhD thesis, Cardiff University.

[40] Ho DT, Kim SY, Schwingenschlögl U. 2020. Graphene origami structures with superflexibility and highly tunable auxeticity. *Phys. Rev. B* **102**, 174106.

[41] Hou Y, Li Z, Wang Z, Yu H. 2021. Miura-ori structured flexible microneedle array electrode for biosignal recording. *Microsystems Nanoeng.* **7**, 53.

[42] Hou Y, Wang Y, Yu M, Wang Z, Yu H. 2020. Miura-ori metastructure enhanced conductive elastomers. *Adv. Mater. Technol.* **5**(8), 2000249.

[43] Kamrava S. 2017. *Origami-based structures with programmable properties*. MSc Thesis, Northeastern University Boston.

[44] Kamrava S, Mousanezhad D, Ebrahimi H, Ghosh R, Vaziri A. 2017. Origami-based cellular metamaterial with auxetic, bistable, and self-locking properties. *Sci. Rep.* **7**, 46046.

[45] Karagiozova D, Zhang J, Lu G, You Z. 2019. Dynamic in-plane compression of Miura-ori patterned metamaterials. *Int. J. Impact Eng.* **129**, 80–100.

[46] Khan KA, Alshaer MH, Khan MA. 2021. A novel twofold symmetry architected metamaterials with high compressibility and negative Poisson's ratio. *Adv. Eng. Mater.* **23**, 2001041.

[47] Kolken HMA, Zadpoor AA. 2017. Auxetic mechanical metamaterials. *RSC Adv.* **7**, 5111–5129.

[48] Lakes RS. 1987. Foam structures with a negative Poisson's ratio. *Science* **235**, 1038–1040.

[49] Lakes RS, Elms K. 1993. Indentability of conventional and negative Poisson's ratio foams. *J. Compos. Mater.* **27**(12), 1193–1202.

[50] Lazarus A, Reis PM. 2015. Soft actuation of structured cylinders through auxetic behavior. *Adv. Rev. Mater.* **17**(6), 815–820.

[51] Lee Y, Kim J, Jang B, Kim S, Sharma BK, Kim JH, Ahn JH. 2019. Graphene-based stretchable/wearable self-powered touch sensor. *Nano Energy* **62**, 197–204.

[52] Lees C, Vincent JF, Hillerton JE. 1991. Poisson's ratio in skin. *Biomed. Mater. Eng.* **1**(1), 19–23.

[53] Lempriere BM. 1968. Poisson's ratio in orthotropic materials. *AIAA J.* **6**(11), 2226–2227.

[54] Li Q, Kuang Y, Zhu M. 2017. Auxetic piezoelectric energy harvesters for increased electric power output. *AIP Adv.* **7**, 015104.

[55] Li Y, Liu W, Deng Y, Hong W, Yu H. 2021. Miura-ori enabled stretchable circuit boards. *npj Flex. Electron.* **5**, 3.

[56] Lin Z, Novelino LS, Wei H, Alderete NA, Paulino GH, Espinosa HD, Krishnaswamy S. 2020. Folding at the microscale: Enabling multifunctional 3D origami-architected metamaterials. *Small* **16**(35), 2002229.

[57] Lira C, Innocenti P, Scarpa F. 2009. Transverse elastic shear of auxetic multi re-entrant honeycombs. *Compos. Struct.* **90**(3), 314–322.

[58] Liu S, Lu G, Chen Y, Leong YW. 2015. Deformation of the Miura-ori patterned sheet. *Int. J. Mech. Sci.* **99**, 130–142.

[59] Luan K, West A, DenHartog E, McCord M. 2019. Auxetic deformation of the weft-knitted Miura-ori fold. *Text. Res. J.* **90**(5–6), 617–630.

[60] Lubarda VA, Meyers MA. 1999. On the negative Poisson ratio in monocrystalline zinc. *Scr. Mater.* **40**(8), 975–977.

[61] Lv C, Krishnaraju D, Konjevod G, Yu H, Jiang H. 2014. Origami based mechanical metamaterials. *Sci. Rep.* **4**, 5979.

[62] Lv Y, Zhang Y, Gong N, Li Z-X, Lu G, Xiang X. 2019. On the out-of-plane compression of a Miura-ori patterned sheet. *Int. J. Mech. Sci.* **161**, 105022.

[63] Meng F, Chen S, Zhang W, Ou P, Zhang J, Chen C, Jong J. 2021. Negative Poisson's ratio in graphene Miura origami. *Mech. Mater.* **155**, 103774.

[64] Misseroni D, Pratapa PP, Liu K, Paulino GH. 2022. Experimental realization of tunable Poisson's ratio in deployable origami metamaterials *Extreme Mech. Lett.* **53**, 101685.

[65] Miura K. 1985. Method of packaging and deployment of large membranes in space. *Inst. Space Astronaut. Sci. Rep.* **618**, 1709–1718.

[66] Mizzi L, Mahdi EM, Titov K, Gatt R, Attard D, Evans KE, Grima JN, Tan J-C. 2018. Mechanical metamaterials with star-shaped pores exhibiting negative and zero Poisson's ratio. *Mater. Des.* **146**, 28–37.

[67] Mizzi L, Salvati E, Spaggiari A, Tan JC, Korsunsky AM. 2020. Highly stretchable two-dimensional auxetic metamaterial sheets fabricated via direct-laser cutting. *Int. J. Mech. Sci.* **167**, 105242.

[68] Mizzi L, Spaggiari A. 2022. Novel chiral honeycombs based on octahedral and dodecahedral Euclidean polygonal tessellations. *Int. J. Solids Struct.* **238**, 111428.

[69] Morvaridi M, Carta G, Bosia F, Gliozzi AS, Pugno NM, Misseroni D, Brun M. 2021. Hierarchical auxetic and isotropic porous medium with extremely negative Poisson's ratio *Extreme Mech. Lett.* **48**, 101405.

[70] Najafi M, Ahmadi H, Liaghat G. 2021. Experimental investigation on energy absorption of auxetic structures. *Mater. Today: Proc.* **34**(1), 350–355.

[71] Novak N, Krstulović-Opara L, Ren Z, Vesenjak M. 2020. Compression and shear behaviour of graded chiral auxetic structures. *Mech. Mater.* **148**, 103524.

[72] Palumbo S, Carotenuto AR, Cutolo A, Owen DR, Deseri L, Fraldi M. 2021. Bulky auxeticity, tensile buckling and deck-of-cards kinematics emerging from structured continua. *Proc. R. Soc. A* **477**, 20200729.

[73] Peng X-L, Soyarslan C, Bargmann S. 2020. Phase contrast mediated switch of auxetic mechanism in composites of infilled re-entrant honeycomb microstructures. *Extreme Mech. Lett.* **35**, 100641.

[74] Prall D, Lakes RS. 1997. Properties of a chiral honeycomb with a Poisson's ratio of -1. *Int. J. Mech. Sci.* **39**, 305–314.

[75] Pratapa PP, Liu K, Paulino GH. 2019. Geometric Mechanics of Origami Patterns Exhibiting Poisson's Ratio Switch by Breaking Mountain and Valley Assignment *Phys. Rev. Lett.* **122**, 155501.

[76] Pratapa PP, Suryanarayana P, Paulino GH. 2018. Bloch wave framework for structures with nonlocal interactions: Application to the design of origami acoustic metamaterials. *J. Mech. Phys. Solids* **118**, 115–132.

[77] Prawoto Y. 2012. Seeing auxetic materials from the mechanics point of view: A structural review on the negative Poisson's ratio. *Comput. Mater. Sci.* **58**, 140–153.

[78] Pydah A, Batra RC. 2017. Crush dynamics and transient deformations of elastic-plastic Miura-ori core sandwich plates. *Thin-Walled Struct.* **115**, 311–322.

[79] Ren X, Das R, Tran P, Ngo TD, Xie YM. 2018. Auxetic metamaterials and structures: a review. *Smart Mater. Struct.* **27**, 023001.

[80] Sareh P, Guest SD. 2014. Designing symmetric derivatives of the Miura-ori. In *Advances in Architectural Geometry*, Springer, 233–241.

[81] Sareh P, Guest SD. 2015. Design of isomorphic symmetric descendants of the Miura-ori. *Smart Mater. Struct.* **24**, 085002.

[82] Sareh P, Guest SD. 2015. A Framework for the Symmetric Generalisation of the Miura-ori. *Int. J. Sp. Struct.* **30**(2), 141–152.

[83] Saxena KK, Das R, Calius EP. 2016. Three decades of auxetics research - materials with negative Poisson's ratio: A review. *Adv. Eng. Mater.* **18**, 11.

[84] Scarpa F. 2008. Auxetic materials for bioprostheses. *IEEE Signal Proc. Mag.* **25**(5), 125–128.

31

[85] Scarpa F, Blain S, Lew T, Perrott D, Ruzzene M, Yates J. 2007. Elastic buckling of hexagonal chiral cell honeycombs *Compos. Part A - Appl. Sci.* **38**(2), 280–289.

[86] Scarpa F, Ciffo LG, Yates JR. 2003. Dynamic properties of high structural integrity auxetic open cell foam. *Smart Mater. Struct.* **13**(1), 49.

[87] Schenk M, Allwood JM, Guest SD. 2011. Cold gas-pressure folding of Miura-ori sheets. In *Steel Research International, Special Issue Proceedings of the International Conference on Technology of Plasticity (ICTP)*, 459–464.

[88] Schenk M, Guest SD. 2013. Geometry of Miura-folded metamaterials. *Proc. Natl. Acad. Sci.* **110**(9), 3276–3281.

[89] Seetoh IP, Leong B, Yi EL, Markandan K, Kanaujia PK, Lai CQ. 2022. Extremely stiff and lightweight auxetic metamaterial designs enabled by asymmetric strut cross-sections. *Extreme Mech. Lett.* **52**, 101677.

[90] Shan S, Kang SH, Zhao Z, Fang L, Bertoldi K. 2015. Design of planar isotropic negative Poisson's ratio structures. *Extreme Mech. Lett.* **4**, 96–102.

[91] Shen J, Zhou S, Huang X, Xie YM. 2014. Simple cubic three-dimensional auxetic metamaterials. *Phys. Status Solidi b* **251**(8), 1515–1522.

[92] Soleimani H, Goudarzi T, Aghdam MM. 2021. Advanced structural modeling of a fold in Origami/Kirigami inspired structures. *Thin-Walled Struct.* **161**, 107406.

[93] Spadoni A, Ruzzene M. 2012. Elasto-static micropolar behavior of a chiral auxetic lattice. *J. Mech. Phys. Solids* **60**(1), 156–171.

[94] Sutton MA, Orteu JJ, Schreier H. 2009. *Image correlation for shape, motion and deformation measurements: basic concepts, theory and applications.* Springer.

[95] Taylor M, Francesconi L, Gerends M, Shanian A, Carson C, Bertoldi K. 2014. Low porosity metallic periodic structures with negative Poisson's ratio. *Adv. Mater.* **26**(15), 2365–2370.

[96] Theocaris P, Stavroulakis G, Panagiotopoulos P. 1997. Negative Poisson's ratios in composites with star-shaped inclusions: a numerical homogenization approach. *Arch. Appl. Mech.* **67**, 274–286.

[97] Timmins LH, Wu Q, Yeh AT, Moore JE, Greenwald SE. 2010. Structural inhomogeneity and fiber orientation in the inner arterial media. *Am. J. Physiol. Heart Circ. Physiol.* **298**(5), 1537–1545.

[98] Ting TCT, Chen T. 2005. Poisson's ratio for anisotropic elastic materials can have no bounds. *Quart. J. Mech. Appl. Math.* **58**(1), 73–82.

[99] Tolman SS, Delimont IL, Howell LL, Fullwood DT. 2014. Material selection for elastic energy absorption in origami-inspired compliant corrugations. *Smart Mater. Struct.* **23**(9), 094010.

[100] Veronda DR, Westmann RA. 1970. Mechanical characterization of skin-finite deformations. *J. Biomech.* **3**(1), 111–122.

[101] Wagner M, Chen T, Shea K. 2017. Large shape transforming 4D auxetic structures. *3D Print. Addit. Manuf.* **4**(3), 133–142.

[102] Wang Z, Hu H. 2014. Auxetic materials and their potential applications in textiles. *Text. Res. J.* **84**(15), 1600–1611.

[103] Wang Z, Luan C, Liao G, Liu J, Yao X, Fu J. 2020. Progress in auxetic mechanical metamaterials: Structures, characteristics, manufacturing methods, and applications. *Adv. Eng. Mater.* **22**, 2000312.

[104] Wei ZY, Guo ZV, Dudte L, Liang HY, Mahadevan L. 2013. Geometric mechanics of periodic pleated origami. *Phys. Rev. Lett.* **110**(21), 215501.

[105] Wickeler AL, Naguib HE. 2020. Novel origami-inspired metamaterials: Design, mechanical testing and finite element modelling. *Mater. Des.* **186**, 108242.

[106] Xiang X, Qiang W, Hou B, Tran P, Lu G. 2020. Quasi-static and dynamic mechanical properties of Miura-ori metamaterials. *Thin-Walled Struct.* **157**, 106993.

[107] Xiang XM, Lu G, Ruan D, You Z, Zolghadr M. 2017. Large deformation of an arc-Miura structure under quasi-static load. *Compos. Struct.* **182**, 209–222.

[108] Xiang XM, You Z, Lu G. 2018. Rectangular sandwich plates with Miura-ori folded core under quasi-static loadings. *Compos. Struct.* **195**, 359–374.

[109] Yang W, Li Z-M, Shi W, Xie B-H, Yang M-B. 2004. Review on auxetic materials. *J. Mat. Sci.* **39**, 3269–3279.

[110] Yasuda H, Yang J. 2015. Reentrant origami-based metamaterials with negative Poisson's ratio and bistability. *Phys. Rev. Lett.* **114**, 185502.

[111] Zhai Z, Wang Y, Lin K, Wu L, Jiang H. 2020. In situ stiffness manipulation using elegant curved origami. *Sci. Adv.* **6**, eabe2000.

[112] Zhang C, Yang Q, Tao R. 2021. Origami-based metamaterial with switchable abnormal expansion function. *Smart Mater. Struct.* **30**, 075004.

[113] Zhang J, Li T, Wang C, Yan X. 2021. Aerodynamic drag characteristics of Miura-ori composite structure. *J. Aerosp. Eng.* **34**(4), 6021004.

[114] Zhang XC, An CC, Shen ZF, Wu HX, Yang WG, Bai JP. 2020. Dynamic crushing responses of bio-inspired re-entrant auxetic honeycombs under in-plane impact loading. *Mater. Today Commun.* **23**, 100918.

[115] Zhang XY, Ren X, Zhang Y, Xie YM. 2022. A novel auxetic metamaterial with enhanced mechanical properties and tunable auxeticity. *Thin-Walled Struct.* **174**, 109162.

Appendix A. Effect of out-of-plane displacements

The finite structure illustrated in Fig. 2(a) exhibits out-of-plane displacements when stretched in the y-direction. The colour map of the displacement component w along the z-axis, given in Fig. A.1, shows that the maximum deflection occurs in the middle part of the system, with zero out-of-plane displacements at the ends, in agreement with the imposed boundary conditions.

The out-of-plane deflection does not affect the in-plane auxetic properties of the folded structure. In order to demonstrate this statement, another numerical simulation is carried out, where the displacements along the z-direction of the lowermost vertices of the folded region are prevented. The resulting displacement fields are presented in Fig. A.2. From the comparison of Figs. A.1 and A.2(c), it is apparent that in the latter case the out-of-plane displacements w are smaller, as expected. However, the in-plane displacements v and u do not vary significantly when the additional constraints are applied (compare parts (a) and (b) of Figs. 5 and A.2). This numerical evidence confirms that, for a linear elastic material subjected to small displacements, the in-plane and out-of-plane behaviours are uncoupled.
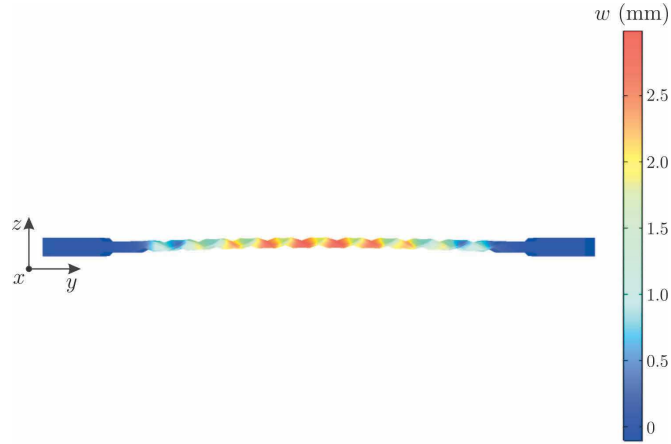
Figure A.1: Colour map of the displacement component along the z-direction (the colour maps of the in-plane displacements of the same finite element model are presented in Fig. 5).

Appendix B. Non-linear analysis

Here, geometrical non-linearities are included into the formulation and the material is assumed to be Neo-Hookean, with $\lambda = 2622.8$ MPa and $\mu = 1124.1$ MPa. The initial geometry is characterised by $a = b = 10$ mm, $t = 0.35$ mm, $\eta_1 = 125°$ and $\eta_2 = 50°$. As shown in Fig. B.1(a), the displacements of the bottom face are prevented, and a uniform stress along the y-direction is applied at the top face, where P is the resulting load. The deformed shape of the structure is illustrated in Fig. B.1(b) with different views; the maximum displacement is denoted by v_{max}.

The relationship between the external load P and the maximum displacement in the y-direction v_{max} is plotted in Fig. B.2(a); the diagram is clearly non-linear, because of the considered geometrical and material non-linearities. Figure B.2(b) shows how the Poisson's ratio ν_{yx} varies with v_{max}, exhibiting a monotonically increasing trend (decreasing in absolute value). This tendency seems to be in contrast with the experimental results illustrated in the video included in the Supplementary Material, where the absolute value of the (negative) Poisson's ratio increases with the longitudinal displacement. However, the experimental outcomes in the non-linear regime are dominated by the effect of damage, which needs to be unavoidably incorporated in the numerical analysis to thoroughly describe the non-linear mechanical behaviour of the folded structure.
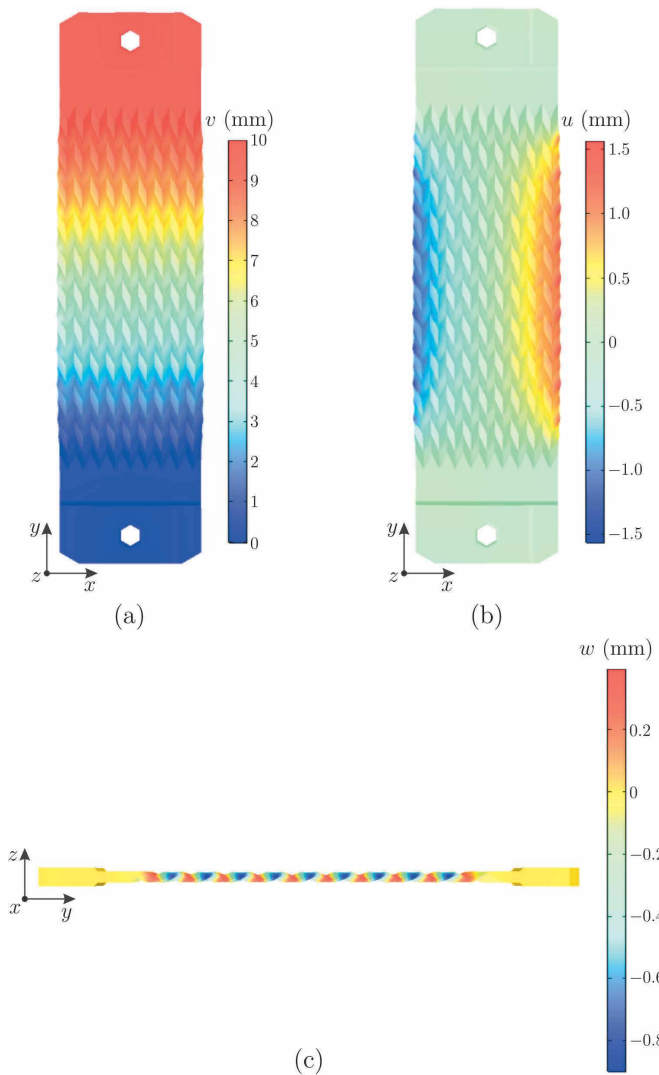
Figure A.2: Colour maps of the displacement components along the (a) y-, (b) x- and (c) z-directions for the finite structure of Fig. 2(a), subjected to an imposed displacement $v_0 = 10$ mm and with zero w displacements imposed at the bottommost vertices of the folded region.
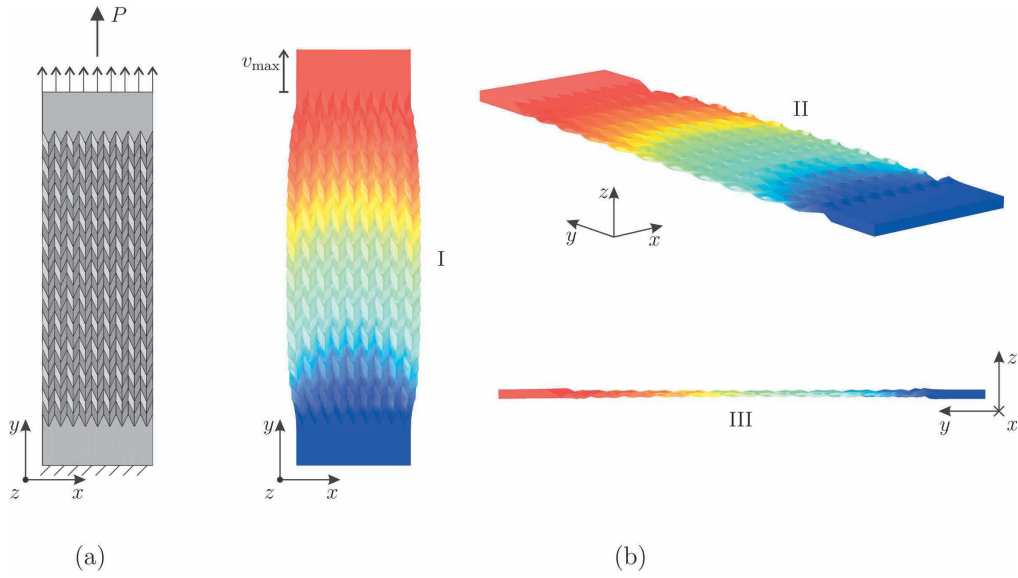
Figure B.1: (a) Schematic representation of the non-linear model, with zero displacements at the bottom face and external traction at the top one. (b) Deformed configuration in (I) top, (II) 3D and (III) lateral view; the colour scale indicates the total displacement field, where the maximum (minimum) value is represented in red (blue) colour.
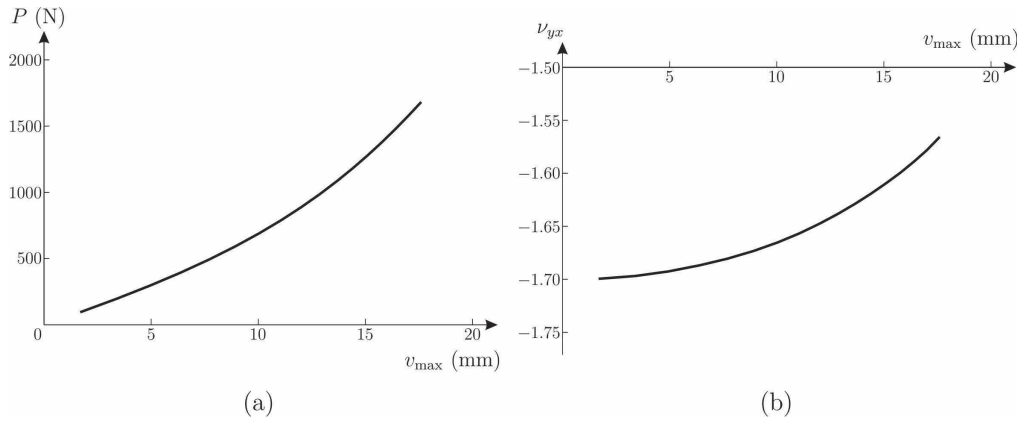

Figure B.2: (a) Curve of applied load versus maximum displacement along the y-axis. (b) Evaluation of Poisson's ratio ν_{yx} as function of the maximum displacement v_{max}.